# Two perspectives on amplified warming over tropical land

Suqin Q. Duan,[a] Karen A. McKinnon,[a,b] and Isla R. Simpson[c]

[a] *Institute of the Environment and Sustainability, University of California, Los Angeles, Los Angeles, CA 90095, USA*

[b] *Departments of Statistics and Data Science, and Atmospheric and Oceanic Sciences, University of California, Los Angeles, Los Angeles, CA 90095, USA*

[c] *Climate and Global Dynamics Laboratory, National Center for Atmospheric Research, Boulder, CO 80307, USA*

*Corresponding author*: Suqin Duan, sqduan@ucla.edu

ABSTRACT: Climate change projections show amplified warming associated with dry conditions over tropical land. We compare two perspectives explaining this amplified warming: one based on tropical atmospheric dynamics, and the other focusing on soil moisture and surface fluxes. We first compare the full spatiotemporal distribution of changes in key variables in the two perspectives under a quadrupling of $CO_2$ using daily output from the CMIP6 simulations. Both perspectives center around the partitioning of the total energy/energy flux into the temperature and humidity components. We examine the contribution of this temperature/humidity partitioning in the base climate and its change under warming to rising temperatures by deriving a diagnostic linearized perturbation model that relates the magnitude of warming to (1) changes in the total energy/energy flux, (2) the base-climate temperature/humidity partitioning, and (3) changes in the partitioning under warming. Using CMIP6 output, we show that the spatiotemporal structure of warming is well predicted by the inverse of the base-climate partition factor, which we term the base-climate sensitivity: conditions that are drier in the base climate have a higher base-climate sensitivity and experience more warming. On top of this relationship, changes in the partition factor under intermediate (between wet and dry) surface conditions further enhance or dampen the warming. We discuss the mechanistic link between the two perspectives by illustrating the strong relationships between lower tropospheric temperature lapse rates, a key variable for the atmospheric perspective, and surfaces fluxes, a key component of the land surface perspective.

SIGNIFICANCE STATEMENT: Understanding what conditions give rise to the largest magnitude of warming in response to rising $CO_2$ concentrations is not only scientifically important but also critical from a climate impacts standpoint. Two main perspectives, one focusing on atmospheric dynamics and the other focusing on land surface processes, have been proposed to explain the stronger warming associated with drier conditions in the tropics. Here, we compare and contrast these two perspectives. Using climate model output, we demonstrate that amplified warming can largely be predicted from base-climate dryness alone in both perspectives, but is further modified based on changes in the partitioning of energy between temperature and moisture. We highlight the spatiotemporal conditions where assumptions in the two perspectives hold and where deviations occur.

## 1. Introduction

The manner in which temperatures are expected to change regionally with global warming is not only an important scientific question, but also a critical issues for climate change impacts and adaptation. Previous studies using climate models have shown that land warms more than the ocean (e.g., Sutton et al. 2007; Joshi et al. 2008, 2013; Byrne and O′Gorman 2013, 2018) and, over tropical land, days at high temperature percentiles warm more than the average, resulting in an elongated upper tail and exacerbated hot extremes (e.g., Duan et al. 2020; Byrne 2021). This "amplified" warming over land seems to be associated with drier conditions: land is drier than the ocean, and those days at the high percentiles of the temperature distribution are days with dry soils and low relative humidity.

Two main perspectives have been proposed to explain this drier–warmer relationship. One perspective is based on tropical atmospheric dynamics (Joshi et al. 2013; Byrne and O′Gorman 2013, 2018). Weak temperature gradients in the tropical upper troposphere (WTG; Sobel and Bretherton 2000) lead to approximately spatially-uniform temperatures. Below, the uniform free tropospheric temperatures are connected to the surface by a temperature lapse rate closer to a moist adiabat over a moist surface such as the ocean and closer to a dry adiabat over a drier surface such as the land. The larger lapse rate over the drier surface corresponds to higher surface air temperature. Upon warming, the moist adiabatic lapse rate reduces, while the dry adiabatic lapse rate does not change; this, combined with the lack of temperature gradients in the free troposphere,

enhances the base-climate temperature gradient across land and ocean and leads to a land-ocean warming contrast (Joshi et al. 2013, the schematics are reproduced in Fig. 1a).

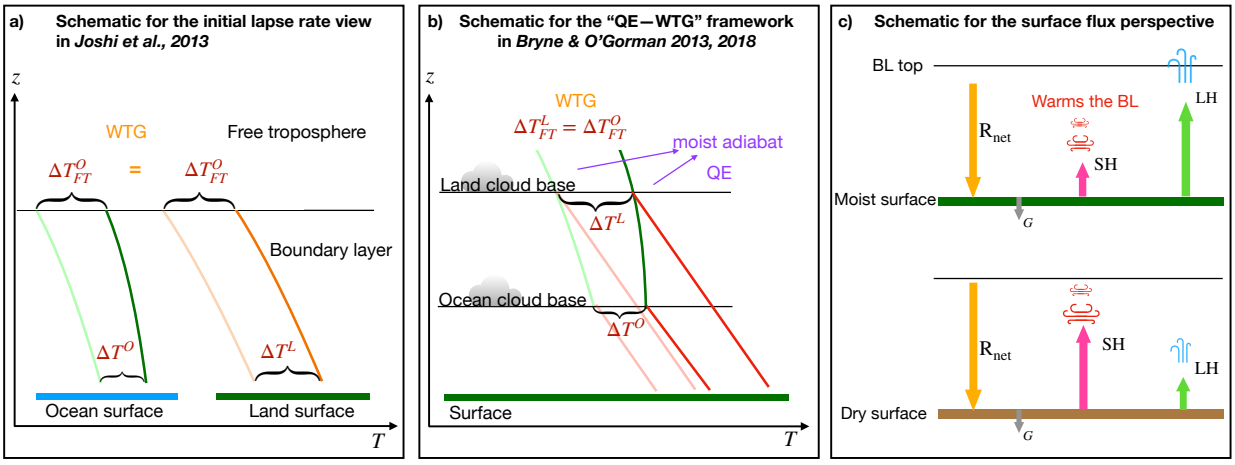


FIG. 1. (a, b) Schematics of cited studies that explain the amplified warming over land with the atmospheric dynamics perspective. In (a) and (b), lines with faint colors show temperature profiles in the base climate; and lines with bright colors show temperature profiles in the warm climate.

Building upon this argument, Byrne and O'Gorman (2013) made the arguments of Joshi et al. (2013) more quantitative by using the concept of quasi-equilibrium (QE; Arakawa and Schubert 1974; Emanuel et al. 1994; Neelin and Zeng 2000). QE together with WTG suggests that the temperature profile in the free tropical troposphere approximately follows the moist adiabat with minimal horizontal gradients. Below the cloud base in the boundary layer, the temperature profile follows a dry adiabat (schematics shown in Fig. 1b). The higher the cloud base, the longer path in the lower troposphere where temperature follows the dry adiabat, the warmer the surface.

With the theoretical bases of QE and WTG, this framework (the "QE–WTG" framework hereafter) can be expressed into mathematical forms by making two assumptions: (1) an atmospheric dynamics constraint that the increase of the boundary layer moist static energy (MSE) across land and ocean is uniform, and (2) a moisture constraint that the change of $q$ over land is a fraction ($\gamma$) of that over ocean. This fraction $\gamma$ comes from the base-climate ratio of $q$ over land to $q$ over ocean, and is assumed to remain constant with climate change. Because the base-climate humidity ratio $\gamma$ is on average less than 1, land moistens less and warms more than the ocean. This "QE–WTG" framework was initially applied to explain the mean warming contrast over land and ocean (Byrne

and O′Gorman 2013, 2018), and has since been adjusted to explain the amplified warming of the hot tail of the temperature distribution over tropical land (Byrne 2021).

In contrast to the atmospheric dynamics based perspective is a land surface based perspective. The surface perspective instead emphasizes changes in the partitioning between sensible and latent heat fluxes in response to moisture availability and/or changes in plants' physiology (e.g., Seneviratne et al. 2010; Berg et al. 2014; Donat et al. 2017; Vogel et al. 2017; Duan et al. 2020; Dirmeyer et al. 2021). When sufficient water is available for evapotranspiration, a greater portion of the net radiation at the surface ($R_n$) is released as latent heat (LH), which does not directly increase the surface air temperature (schematic in Fig. 1c). When the soil gets sufficiently dry and/or plants' stomata close, the ratio of $R_n$ that can be released through LH reduces. Consequently, the surface warms more and sensible heat (SH) fluxes increases, which warms the near-surface air. In this surface perspective, soil moisture, or the Bowen ratio (the ratio of SH to LH) critically controls the warming magnitude.

Although both perspectives involve a partition of the total energy between moistening and warming, there is a gap between the perspectives. The atmospheric perspective is used primarily by the atmospheric dynamics community, and its reasoning relies on constraints that are end products of atmospheric variables in an equilibrium state without explicit links to the changes in soil moisture or vegetation dynamics that the surface perspective emphasizes. In fact, the moisture constraint in the QE-WTG framework is derived from an "ocean influence model" (Chadwick et al. 2016; Byrne and O′Gorman 2016, 2018). The surface perspective is familiar to the land-atmosphere interaction community, and is process-based, but the physical constraints are based on the local surface energy balance and there is a lack of connection to atmospheric processes and to the global constraints offered by the atmospheric dynamics perspective. Furthermore, the atmospheric perspective has mainly been invoked to explain large-scale (e.g. averaged across zonal bands and/or over land and ocean) and time-mean changes (only recently applied to daily time scales; Byrne 2021); whereas the surface perspective has widely been used for local extreme days (e.g., Donat et al. 2017; Vogel et al. 2017; Duan et al. 2020; Dirmeyer et al. 2021).

In addition, there is a nuanced question regarding whether the climatological dryness, or the change in dryness in response to increased $CO_2$, is more important for amplified warming (dryness is measured by specific humidity in the atmospheric perspective and soil moisture in the surface

perspective). In the QE–WTG framework, the moisture constraint parameter $\gamma$ is calculated based on the base-climate specific humidity alone, i.e., the amplified warming can be predicted for regions that are climatologically dry (base-climate $\gamma$ smaller than one), whereas the surface perspective often emphasizes *changes* in the soil moisture or surface flux partition with climate change. This difference can cause confusion especially when the decrease of relative humidity (RH) or the increase of climate aridity (measured by P/PET in the cited work) are discussed together with the amplified warming (Sherwood and Fu 2014; Fu and Feng 2014; Byrne and O′Gorman 2018): one may wonder whether more drying leads to more warming, or more warming leads to more drying.

In order to understand the equivalency, or lack thereof, between the two perspectives, we examine the following questions in the context of climate models:

(1) Do the key variables in the two perspectives correspond to each other?

(2) How do the dryness measures between the two perspectives relate to each other?

(3) How do climatological dryness versus changes in dryness contribute to amplified warming in each perspective?

Motivated by these questions, we first compare the full spatiotemporal distribution of key variables and their changes in the two perspectives using a process-based phase space of daily soil moisture and the climatological aridity index, which captures both the temporal variability and the climatological spatial variations in dryness (Duan et al. 2023). In the phase space, we can visualize how each perspective manifests both across climatologically dry and wet regions as measured by the climatological aridity index (AI), and across temporal variability in dryness and wetness within locations that have similar AIs. The data and frameworks we use are introduced in Section 2. We discuss the applicability of the QE-WTG framework to explaining the spatiotemporal distribution of warming and examine the moisture constraint's connection with the land surface in Section 3. We then use a diagnostic linearized perturbation model (see also Zeppetello et al. 2020; Chan et al. 2022, for applications in land-atmosphere interactions) to discuss the relative roles of the base-climate dryness versus the change in dryness for the magnitude of warming in Section 4. This linearized perturbation model also offers an alternative way to view the connection of the two perspectives. We briefly comment on the mechanistic connection of the two perspectives via the association of the lower tropospheric temperature lapse rate to surface flux partition in Section 5 and provide a final summary in Section 6.

## 2. Data and Methods

*Data*

We analyze simulations submitted to the Coupled Model Intercomparison Project Phase 6 (CMIP6; Eyring et al. 2016). We take the first 30 years (1850–1879) in the historical experiment as the control (base) climate state, and years 121–150 in the abrupt-4×$CO_2$ (4×$CO_2$ for short) experiment as the perturbed climate state. Climate changes in variables are characterized by subtracting the base state from the perturbed climate state. We use the outputs from nine models that have reported daily values of near-surface (2 m) air temperature ($T$), specific humidity ($q$), relative humidity (RH), surface soil moisture (SM, moisture in the top 10 cm soil layer), surface latent heat flux (LH), surface sensible heat flux (SH), and upwelling and downwelling shortwave and longwave radiative fluxes from which we calculate the net radiation at the surface ($R_n$, downward positive), for both the historical and 4×$CO_2$ experiments. The nine models are: CanESM5, CMCC-ESM2, GFDL-CM4, MIROC6, IPSL-CM6A-LR, INM-CM5-0, MPI-ESM-1-2-HAM, MPI-ESM1-2-HR, and MRI-ESM2-0. The limitation to these specific nine models mainly comes from the availability of surface soil moisture and surface flux outputs at daily frequency in the 4×$CO_2$ experiment (e.g., daily SM is not available for CESM2, and daily surface and radiative fluxes are not available for the ACCESS and EC-Earth models). Besides the limitation due to the data availability, we only include one model from each modeling institution even if outputs from the different versions of that model are available. In this case, we consider the more recent version, or the higher resolution version that has the more complete set of variables available. NorESM2-MM, FGOALS-g3, TaiESM1 have also reported daily surface soil moisture, but a large amount of the soil moisture values are invalid and therefore they are not included. In addition to the variables listed above, precipitation $P$ in the historical experiment is used in order to calculate the climatological Aridity Index (AI). AI is defined as $\mathrm{AI} = 0.8R_n/(L_vP)$. Arid regions have larger AI under this definition, and the constant 0.8 is set empirically to account for the fact that not all available energy goes into evapotranspiration even if soil moisture is abundant (Milly and Dunne 2016; Koster and Mahanama 2012). To calculate the near surface air moist static energy (MSE, $\mathrm{MSE} = c_pT + L_vq + gz$, where $c_p$ is the specific heat of dry air, $T$ is the surface air temperature, $L_v$ is the latent heat of vaporization, $q$ is the surface air specific humidity, $g$ is the

gravitational acceleration, and $z$ is the height above sea level), we also use the orographic height variable. Since the orographic height will not change with climate change, we only need this $gz$ term when calculating MSE in one climate state. Temperature and geopotential height on pressure levels (variable *ta* and *zg*) during 1850–1879 in the historical experiment are used to calculate the temperature lapse rate between 700 hPa and the surface. Since MRI-ESM2-0 only reports daily 3D variable after 1950, and daily 3D *zg* from CMCC-ESM2 is not available, we use only the remaining seven models for temperature lapse rates and profiles. We use the grid-cell land area fraction variable to select land grid cells as those with a land area fraction $\geq 99\%$. Since we are interested in situations where we expect a strong land surface control on temperature, we focus on the warm season, which we define as the 150 days centered on July 15 for the Northern Hemisphere, and the 150 days centered on Jan 15 for the Southern Hemisphere.

*The daily soil moisture/climatological aridity index (SM/AI) phase space*

The land surface is highly heterogeneous: it ranges from very arid regions such as the Sahara desert to very moist regions such as the Amazon forest. For a given location, temporal variability of dryness/wetness can substantially affect the surface latent heat flux: LH that is more than 150 W/m$^2$ during average days can reduce to only a few tens of W/m$^2$ when the soil is dry (see Fig. A1g). Furthermore, when considering changes of these hydroclimatic variables under climate change, more complexity comes into play due to the non-linear relationship between LH and soil moisture. In particular, for a fixed amount of net radiation at the surface, LH increases with SM in the transitional regime but is not sensitive to SM in the dry and wet regimes (e.g., Seneviratne et al. 2010) and decreases with SM in the active-rain regime (Duan et al. 2023). As a result, when soil dries under climate change, LH decreases in the transitional regime while increases in the wet regime due to increases in net radiation (Duan et al. 2023). These different changes in LH can lead to different responses in surface air temperature: warming will be magnified in the transitional regime due to reductions in latent cooling, in contrast to the behavior in the wet regime. Since places with different climatological dryness have different percentages of days in each of the LH–SM regimes, averaging over time that contains both local wet and dry days, or averaging over locations with different local soil moisture distributions can lead to substantial canceling of signals and result in an averaged behavior that is hard to interpret. Moreover, models represent

the spatiotemporal distribution of soil moisture and the evapotranspiration–soil moisture functions differently, resulting in further uncertainty.

Duan et al. (2023) presented a process-based phase space constructed using daily soil moisture and the climatological aridity index and showed that, when organizing the highly heterogeneous land hydroclimatic variables in this phase space, one can acquire coherent patterns of changes across models and across variables. The coherent patterns in this SM/AI phase space are in contrast to the highly uncertain results in the geographical map view (Fig. S3 of Duan et al. (2023)). Here we adopt this method, and process the model fields that have dimensions of calendar days and geographical locations into phase-space grids consisting of 50 temporal bins and 50 spatial bins. The horizontal axis of the phase space is formed by the temporal bins, and calculated by sorting the original data according to the daily SM and placing 2% of the 4500 days in each bin. These temporal bins represent local dry days to wet days. The vertical axis of the phase space is formed by the spatial bins, and calculated by sorting the original grid cells (for both the base and the $4\times CO_2$ climate states) according to the *base-climate* warm-season mean AI and placing 2% of the tropical land area (30°S–30°N) in each bin. These spatial bins represent the climatologically moist regions to climatologically arid regions. We then take the area-weighted average of data in each bin and plot the bin-average values as shadings. Fig. A1 and Fig. 3 show a number of variables and their changes displayed in this SM/AI phase space. We refer to the average in each of the $50\times 50$ bins as data "under a certain spatial-temporal condition". We normalize changes in variables in the phase space by the tropical mean ocean warming $[\overline{T}]_o$ in each model before averaging over models to accounts for the different climate sensitivities across models.

*The diagnostic linearized model for the magnitude of warming*

Both perspectives consider a partitioning of a total energy (MSE) or energy flux ($R_n$) between a temperature component ($c_pT$ or SH) and a humidity component ($L_vq$ or LH). Here we reduce the variables in the balance relations and rearrange them to relate the temperature component to the total energy/energy flux by a partition factor. When considering climate change, we decompose changes in the total energy/energy flux into a component with an unchanged base-state partition factor and a component representing the contribution from changes in this partition factor. This method of decomposition helps us compare the partitioning in the two perspectives, and diagnose

the relative importance of the base-climate dryness versus the change in dryness under climate change in contributing to the amplified warming over tropical land. Distinguishing between the role of the base climate state and changes to that state is important, because information about the base climate state is also available from observations, and can be used to make predictions and constrain climate change projections. We derive the relations below.

In the surface flux perspective, the total net energy flux received by the surface is the net radiation $R_n$. $R_n$ is largely balanced through the surface sensible heat flux (SH) and the surface latent heat flux (LH), with a small component $G$ going into the ground. In general, the surface energy balance $R_n - G = \mathrm{SH} + \mathrm{LH}$, can be approximated as $R_n \approx \mathrm{SH} + \mathrm{LH}$. The Bowen ratio, $B = \mathrm{SH}/\mathrm{LH}$, summarizes the relative partitioning between SH and LH. When the Bowen ratio is higher, more of the incoming heat goes into SH, which warms the near-surface air. Using $B$, we can write $\mathrm{SH} + \mathrm{LH}$ as $(B+1)B^{-1}\mathrm{SH}$, and then have

$$R_n \approx \mathrm{SH} + \mathrm{LH} = \frac{B+1}{B}\mathrm{SH} = \Psi \mathrm{SH} \tag{1}$$

where $\Psi = (B+1)/B \approx R_n/\mathrm{SH}$. In this way, we associate the total energy flux to SH through a ratio $\Psi$. Below, we link SH to temperature. The inverse, $1/\Psi$, is the fraction of $R_n$ balanced by SH, and is strongly related to the dryness of the surface (i.e., soil moisture).

While the surface flux perspective is based on partitioning of the net radiative flux, the atmospheric dynamics perspective is based on partitioning of the total energy MSE, which is assumed to be uniform across the tropics in QE-WTG theory. Leaving aside the $gz$ term in MSE that will not change under warming, the moist enthalpy ($\mathrm{ME} = c_p T + L_v q$) consists of a temperature component $c_p T$ (the dry specific enthalpy), and a moisture component $L_v q$. By a similar approach to that used above for surface fluxes, we can use the ratio between these two components as $b = (c_p T)/(L_v q)$ to write ME as

$$\mathrm{ME} = \mathrm{MSE} - gz = c_p T + L_v q = \frac{b+1}{b} c_p T = \psi c_p T\,, \tag{2}$$

where $\psi = (b+1)/b = \mathrm{ME}/(c_p T)$. In this way, we associate the total energy to surface air temperature, through a ratio $\psi$. The inverse, $1/\psi$, is the fractional contribution of the temperature component in the total ME. Thus, the surface energy and atmospheric dynamic views can be

written in somewhat comparable forms (see Table 1), and we will compare these parameters and their changes in the remainder of the paper.

Under climate change, the variables in Eqs. 1 and 2 can be expressed as a base state combined with a perturbation ($\Delta$). By dropping the non-linear interaction terms between the perturbations (residuals of the linearization are shown in Fig. B1ab in Appendix B), the equations that govern the atmospheric and land perspectives can be written as,

$$\Delta\mathrm{MSE} = \Delta\mathrm{ME} \approx \psi c_p \Delta T + c_p T \Delta\psi\,, \tag{3}$$

and

$$\Delta R_n \approx \Psi\Delta\mathrm{SH} + \mathrm{SH}\Delta\Psi \tag{4}$$

$$\approx \Psi\kappa\Delta T + \mathrm{SH}\Delta\Psi \tag{5}$$

In Eq. 5, we have assumed that $\Delta\mathrm{SH} = \kappa\Delta T$ where $\kappa$ is a constant i.e., the sensible heat flux anomalies can be linearly related to the temperature anomalies using a proportionality constant, following the concepts in Vargas Zeppetello and Battisti (2020); Chan et al. (2022); Kong et al. (2023). This allows the land perspective to be written in terms of a dependence on $\Delta T$, analogous to the atmosphere perspective. We examine this assumption in more detail and discuss its limitations in Appendix C. It is important to note that MSE is an energy that directly contains the $T$ component, while $R_n$ is a flux balanced by two fluxes that affect and are affected by $T$ and $q$. This leads to a more exact relationship between $\Delta T$ and $\Delta\mathrm{ME}$ in Eq. (3) while a more approximate relationship that relies on an additional parameter, $\kappa$, in Eq. (5).

From here, we can write the temperature change in association with either a change in MSE or $R_n$ as:

$$\Delta T = \frac{\Delta\mathrm{MSE} - c_p T \Delta\psi}{c_p \psi}\,, \tag{6}$$

and

$$\Delta T = \frac{\Delta R_n - \mathrm{SH}\Delta\Psi}{\kappa\Psi}\,. \tag{7}$$

In Eq. 6 and Eq. 7, $\Delta\mathrm{MSE}$ and $\Delta R_n$—change of the total energy or energy flux—can be regarded as analogs of the "forcing" used in studies of climate sensitivity and feedbacks (Roe 2009; Held

and Shell 2012; Zelinka et al. 2020). Because we analyze the changes between two climate states approximately in equilibrium, the "forcing" terms include changes in climate that lead to equilibration, such as increases in upwelling longwave radiation. Therefore, they are a combination of forcing and response, but we can understand these responses of the total energy and energy flux as relatively externally constrained (external to the temperature response), and we analyze the temperature response given these changes in the total energy/energy flux (the forcing analog).

The terms $(c_p\psi)^{-1}$ in Eq. 6 and $(\kappa\Psi)^{-1}$ in Eq. 7 can be understood as the sensitivity of the temperature response to the forcing analog (the total energy/energy flux). The specific heat of dry air, $c_p$, is a physical constant. For simplicity, we also consider $\kappa$ to be a constant as discussed above. Therefore, in the following sections, we take $\psi^{-1}$ and $\Psi^{-1}$ as the sensitivities in each framework, which are solely determined by the base-climate state.

The terms $-c_pT\Delta\psi$ and $-\mathrm{SH}\Delta\Psi$ are the contribution of the change in the partition factor ($\psi$ and $\Psi$, the inverse of which is the sensitivity discussed above) to the magnitude of warming, and we refer to them as the "repartition" terms. Specifically, the terms summarize the *changes* in the partitioning of MSE into $T$ and $q$ for the atmospheric framework, or the partitioning of $R_n$ into SH and LH for the surface energy balance framework. The sign of the repartition terms is consistent with their effect on the temperature response: positive values indicate that the balance is repartitioning in a way that will increase the temperature response, and decrease the moisture response.

A summary of the balance relations, their linearized perturbation equations and relevant terms for the two perspectives are listed in Table 1.

## 3. Comparing the two perspectives across the spatiotemporal distribution

Previous results based on the QE-WTG framework (Byrne and O'Gorman 2013, 2018; Byrne 2021) are often displayed in terms of zonal averages, and results from the surface perspectives (e.g., Donat et al. 2017; Vogel et al. 2017) are often reported as a temporal maxima (or the highest percentiles). Here we compare the full spatiotemporal distribution of key variables in the two perspectives. To do so, we employ the SM/AI phase space as described in Section 2. Recall that in this phase space, the horizontal axis captures temporal variability as measured by local daily soil moisture (SM) percentiles , and the vertical axis captures spatial variability as measured by the

TABLE 1. A summary of the equations and terms considered for the base-climate physics and climate change perturbations in the atmospheric-dynamics and the surface-flux perspectives.

| Constraint | Balance | Partition factor | Derived relation |
|---|---|---|---|
| MSE (ME) | $\mathrm{ME} = \mathrm{MSE} - gz = c_pT + L_vq$ | $b = \frac{c_pT}{L_vq}$, $\psi = \frac{b+1}{b}$ | $\mathrm{ME} = \psi c_pT$ |
| $R_n$ ($R$) | $R = R_n - G = \mathrm{SH} + \mathrm{LH}$ | $B = \frac{\mathrm{SH}}{\mathrm{LH}}$, $\Psi = \frac{B+1}{B}$ | $R = \Psi \mathrm{SH}$ |

| Linearized perturbation relation | $T$ response | Sensitivity | Change of the total | Repartition term |
|---|---|---|---|---|
| $\Delta\mathrm{MSE} \approx \psi c_p \Delta T + c_pT\Delta\psi$ | $\Delta T \approx \frac{\Delta\mathrm{MSE} - c_pT\Delta\psi}{c_p\psi}$ | $\frac{1}{c_p\psi}$ | $\Delta\mathrm{MSE}$ | $-c_pT\Delta\psi$ |
| $\Delta R_n \approx \Psi\kappa\Delta T + \mathrm{SH}\Delta\Psi$ | $\Delta T \approx \frac{\Delta R_n - \mathrm{SH}\Delta\Psi}{\kappa\Psi}$ | $\frac{1}{\kappa\Psi}$ | $\Delta R_n$ | $-\mathrm{SH}\Delta\Psi$ |

climatological Aridity Index (AI) percentiles. The isoline of a surface soil moisture value of 20 kg/m$^2$ is shown as a black contour (solid for the base climate and dashed for the 4×$CO_2$ climate). This line roughly indicates the critical soil moisture, $\mathrm{SM_{crit}}$, that marks the transitional regime in the Budyko curve where soil moisture limits evapotranspiration and the soil moisture-temperature feedback is the strongest. While its specific value can vary across models, time, and region, this value can be used as a rough indicator in CMIP6 models (Duan et al. 2023). To the lower-right of this line are wetter conditions, both spatially and temporally, and to the upper-left are drier conditions.

### *a. The atmospheric perspective*

In the atmospheric perspective, change of the total energy (ΔMSE, Fig. 2a) is split, by definition, between warming ($c_p\Delta T$, Fig. 2b) and moistening ($L_v\Delta q$, Fig. 2c). ΔMSE (Fig. 2a) shows an increase across all 50 × 50 temporal and spatial bins with a value ranging from 3.3 to more than 4.2 kJ/kg per degree of mean tropical ocean warming. The warming magnitude ($\Delta T$, Fig. 2b) is smaller in moist conditions (lower right) while it is larger in dry conditions (upper left), maximizing over the desert regions. Warming around the critical soil moisture contours in moist regions is also strong, and this amplified warming center around $\mathrm{SM_{crit}}$ is more evident in changes of the

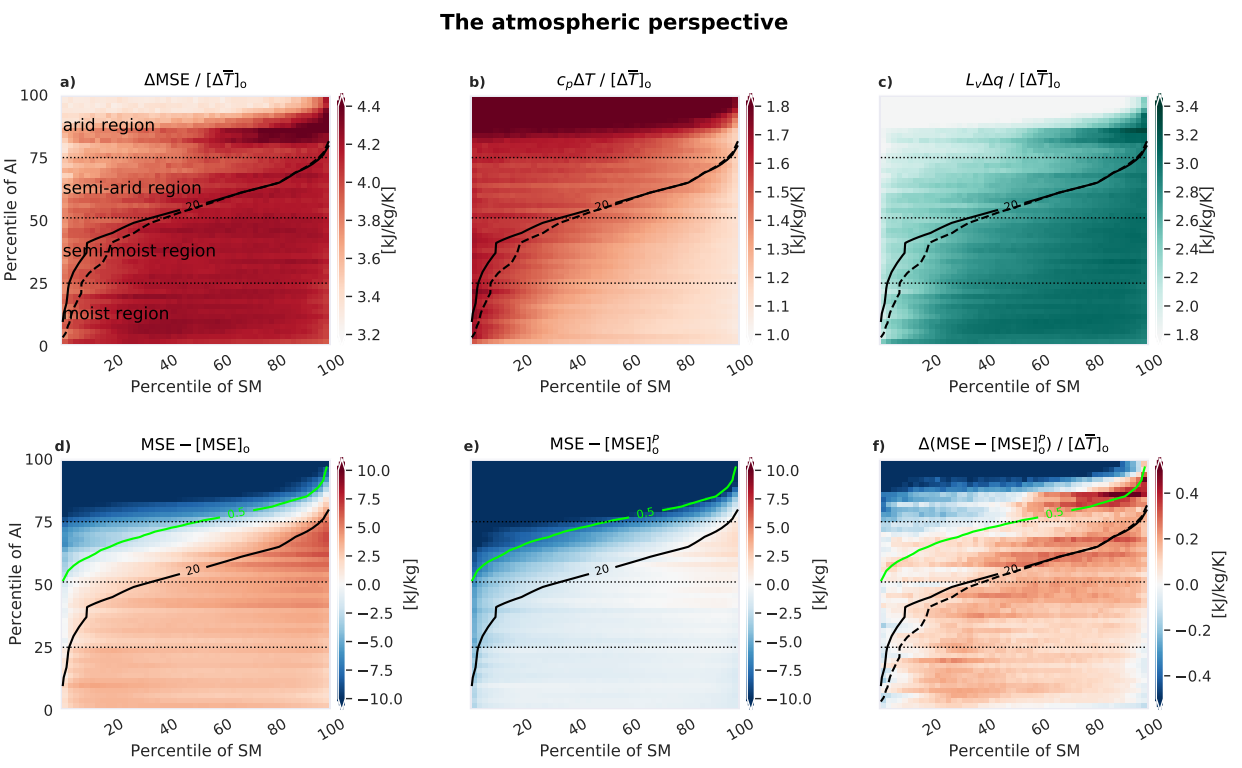


FIG. 2. Changes in the surface air (a) moist static energy (MSE), (b) temperature converted to energy units ($c_pT$), (c) specific humidity converted to energy units ($L_vq$), between the $4\times CO_2$ climate state and the base climate state displayed in the phase space of daily soil moisture percentiles (horizontal axis), and climatological Aridity Index percentiles (vertical axis). (d) Deviation of the moist static energy (MSE) over land from the corresponding (corresponding day and latitude) zonal mean values over the ocean ($[\text{MSE}]_o$) in the base climate; (e) deviation of the MSE over land from the corresponding precipitation-weighted zonal mean values over the ocean ($[\text{MSE}]_o^P$) in the base climate, (f) changes of the deviation of the land MSE from $[\text{MSE}]_o^P$ between the $4\times CO_2$ climate state and the base climate state. Changes of variables are normalized by the mean tropical ocean warming $[\Delta\overline{T}]_o$ in each model before averaging over the models. The black contours (solid for the base climate and dashed for the $4\times CO_2$ climate) are the isolines of the surface soil moisture value of 20 kg/m$^2$ which roughly marks the conditions in the transitional regime of the Budyko curve. The green contour is the isoline of the daily mean precipitation rate of 0.5 mm/day. See text for more details.

daily-maximum temperature (not shown). Specific humidity $q$ increases under all conditions, and the magnitude is generally contrary to that of $\Delta T$, i.e., wetter conditions moisten more and warm less, while drier conditions moisten less and warm more.

Mathematically, the QE–WTG framework (Byrne and O′Gorman 2013, 2018; Byrne 2021) predicts warming over land as:

$$\begin{aligned}\Delta T^L &= (\Delta \mathrm{MSE}^L - L_v \Delta q^L)/c_p = (\Delta \mathrm{MSE}^O - \gamma L_v \Delta q^O)/c_p \\ &= \Delta T^O + (1-\gamma)\frac{L_v}{c_p}\Delta q^O \end{aligned} \tag{8}$$

In this equation, the super-script $L$ and $O$ denote land and ocean, as in the original work. $\gamma$, as mentioned in the Introduction, is the ratio of $q^L$ to its corresponding zonal mean value over the ocean in the base climate ($\gamma = q^L/q^O$). $\gamma$ is assumed to be constant with climate change and therefore $\Delta q^L = \gamma \Delta q^O$.

In the QE–WTG framework, $\Delta$MSE is generally assumed to be uniform across various divisions of the tropics. For example, Byrne and O′Gorman (2013, 2018) assumed uniform annual-mean changes across land and ocean for a given latitude, and Byrne (2021) showed uniform changes in CMIP6 models for the upper 50 MSE percentiles across time and locations over land and ocean. With this assumption, amplified warming is then predicted in conditions with less moistening. The general "less moistening–more warming" correspondence we see in Fig. 2b and Fig. 2c seem to be consistent with the theory of this QE-WTG framework. However, it is interesting to note that we also see the less moistening-more warming relationship over the desert, despite the fact that there is almost no moist convection over the desert, so the region is not expected to be in convective quasi-equilibrium as required by the theory. Indeed, as we can see in Fig. 2a, the change in MSE is noticeably smaller in deserts than other regions, since there is a lack of coupling between the desert boundary layer and other regions that are dominated by moist convection. Thus, the assumption of equal change in MSE that has been applied previously to other groupings of regions in the tropics appears to break down in the phase space we consider, particularly in the drier days and regions that warm the most.

To further test the QE–WTG framework regarding the assumption about the uniform MSE in the AI/SM phase space, we compare the MSE at a certain spatiotemporal condition over land to the corresponding day and latitude zonal mean values over ocean in the base climate in Fig. 2d. If all conditions satisfy QE and WTG (especially QE, since WTG holds relatively well across locations in the tropics, see Fig. 6c), the values in Fig. 2d should be approximately zero, indicating that MSE over

land roughly equals the corresponding value over the ocean. However, Fig. 2d shows greater-than-zero values for wet conditions and less-than-zero values for dry conditions. Zhang and Fueglistaler (2020) showed that this equal-MSE assumption holds better when conditioned on precipitating situations (we refer to this as the revised equal-MSE assumption below). Following their approach, Fig. 2e shows the MSE at each location over land with the corresponding *precipitation-weighted* zonal mean values over ocean ($[\mathrm{MSE}]_o^P$) subtracted. We can see that most of the moist conditions (to the right of the black line of the $\mathrm{SM_{crit}}$, or the green isoline of the precipitation rate 0.5 mm/day) approximately satisfy the revised equal-MSE assumption. For dry conditions, land MSE still deviates from $[\mathrm{MSE}]_o^P$ by more than 10 kJ/kg. This deviation is expected because, as mentioned above, these very dry conditions do not satisfy the QE assumption that relies on active moist convection.

QE-WTG suggests equal MSE over land and ocean in each of the base and the warm climate states, from which the equal *change* of MSE over land and ocean is derived. Fig. 2f shows changes of the MSE deviation from the precipitation-weighted ocean zonal mean value over land between the warm and the base climate states, i.e., $\Delta(\mathrm{MSE}-[\mathrm{MSE}]_o^P)$. Note that even in the moist conditions where the difference between land and ocean is close to 0 in the base climate (to the lower right of the black line in Fig. 2e), the MSE increase over land with climate change is still larger than the increase over the precipitating ocean. The magnitude of this deviation (difference between MSE increases over land and ocean) can be as large as 0.3–0.5 kJ/kg (0.3–0.5 K in temperature units) for each degree of tropical mean ocean warming. Thus, while these assumptions are necessary to form the over-arching theory of QE–WTG, and have been used to successfully explain the behavior of climatological averages over large domains (e.g. land and ocean averages), their accuracy diminishes when considering the spatiotemporal distribution in this manner. In applying the QE-WTG framework to extreme temperature at the daily time scale, Byrne (2021) added a term ($\Delta h$) to address the smaller changes in MSE during hot days over land that are evident in our phase space (Fig. 2f).

### *b. The surface perspective*

For the surface flux perspective, changes in the total energy flux, i.e., the net radiation at the surface ($R_n$; Fig. 3a) are partitioned between changes in the surface sensible heat flux ($\Delta$SH, Fig. 3b)

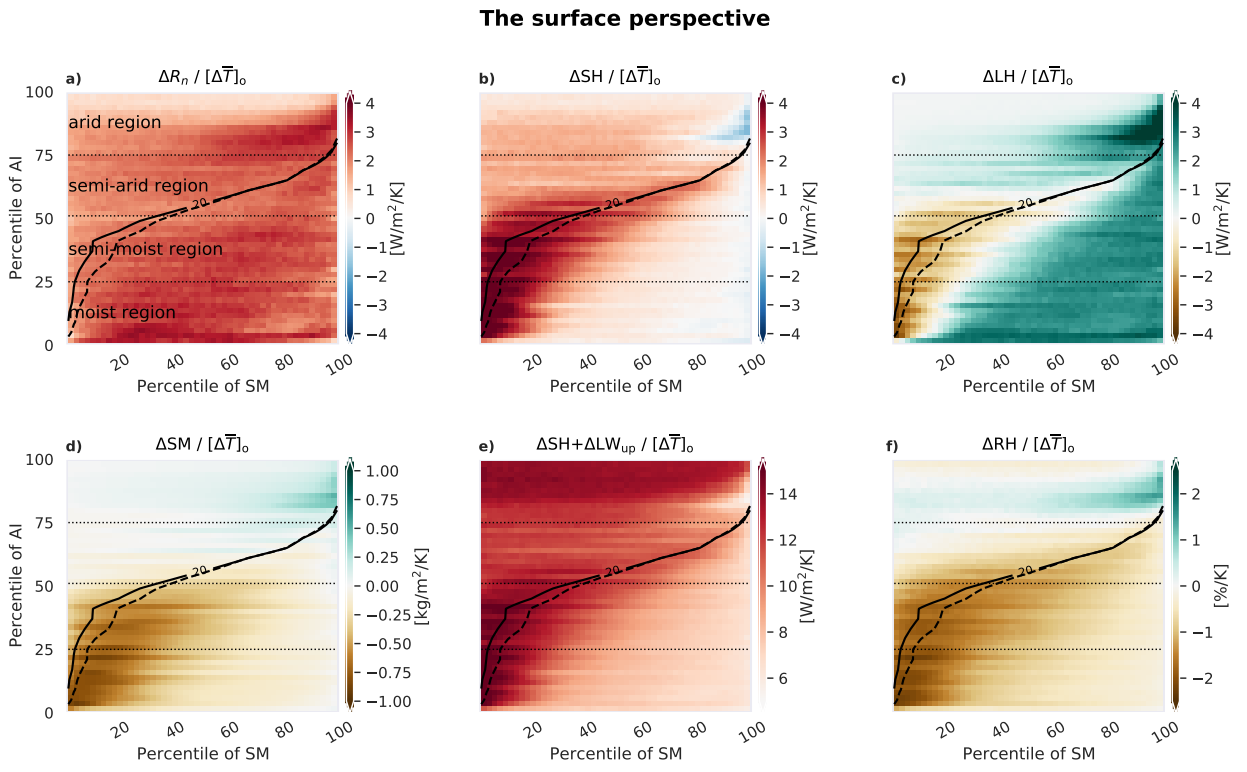


385 FIG. 3. Changes in the surface air (a) surface net radiation ($R_n$), (b) surface sensible heat flux (SH), (c) surface
386 latent heat flux (LH), and (d) soil moisture (SM), (e) SH plus upwelling longwave radiation (SH + $LW_{up}$), and (f)
387 relative humidity (RH) between the $4\times CO_2$ climate state and the base climate state, displayed in the phase space
388 of daily soil moisture percentiles (horizontal axis), and climatological Aridity Index percentiles (vertical axis).
389 Changes in these variables are normalized by the mean tropical ocean warming $[\Delta\overline{T}]_o$ in each model before
390 averaging over the models. The black contours (solid for the base climate and dashed for the $4\times CO_2$ climate) are
391 the isolines of the surface soil moisture value of 20 kg/m$^2$ which roughly marks the conditions in the transitional
392 regime. See text for more details.

395 and changes in the surface latent heat flux (ΔLH, Fig. 3c), with a negligible change in ground heat
396 fluxes (not shown). $R_n$ increases under all spatiotemporal conditions of dryness and wetness,
397 with the maximum increase in wet conditions (around 3 W/m$^2$ per degree of ocean warming) and
398 smallest increase over the desert (around 1 W/m$^2$ per degree of ocean warming). The pattern
399 of $\Delta R_n$ across the spatiotemporal states is highly similar to the pattern of ΔMSE (Fig. 2a); their
400 correlation across the 2500 bins in the phase space is 0.85. This close correspondence between
401 the changes in the total energy in the surface air and changes in the total energy flux at the surface

may be explained by the following two possibilities: one is that increases in $R_n$ drive the increases in MSE; the other is that increases in $q$ (Fig. 2c), which is the dominant component in ΔMSE (Fig. 2a), result in increases in $R_n$ through the increased radiative emissivity of moister air.

Except for the very dry conditions where changes in LH are near-zero, and the transitional conditions around $SM_{crit}$ where LH decreases and SH increases, changes in $R_n$ are predominantly balanced by increases in LH. In particular, in the wet conditions (those to the right of $SM_{crit}$), LH increases by about 2–3 W/m$^2$ per degree of mean ocean warming, while SH changes much less (or even decreases), by ±1 W/m$^2$ per degree of mean ocean warming. Recall that, in these same moist locations and times, increases in specific humidity also dominate the increases in MSE, and the warming magnitude is similar to that over ocean (Fig. 2b).

For the transitional conditions around $SM_{crit}$, decreases in LH are substantial (Fig. 3c). The decrease in LH is driven by drying of SM (Fig. 3d, also indicated by shift of the $SM_{crit}$ isoline to higher percentiles), and is compensated by strong increases in SH. The increase in SH and decrease in LH in the transitional conditions correspond to amplified warming in these conditions (Fig. 2b), reflecting the role of surface flux repartitioning in exacerbating the warming. It is interesting to note, however, that even though LH decreases in these transitional conditions, specific humidity increases (Fig. 2c). This reflects the role of other sources and sinks of surface air specific humidity besides the local land surface evapotranspiration. Meanwhile, RH decreases (Fig. 3f), suggesting that specific humidity has not increased enough to match the increase in the saturation specific humidity. RH is often taken as a reflection of the atmospheric dryness; the decrease of RH along $SM_{crit}$ despite the increase of the specific humidity indicates that soil moisture–temperature feedback is an important contributor to the decrease of RH over land.

In arid regions (upper quarter of the phase space), in the base climate state, LH is small (deserts are dry) and $R_n$ is predominantly balanced by SH. With climate change, changes in LH will be small (deserts remain deserts) and we might expect large increases in SH, corresponding to the pronounced warming (Fig. 2a). However, we see here that changes in SH in these arid regions are also small. This is because both the surface and near surface air warm substantially, and the increase of long wave radiation (which scales with $T^4$) is faster than the increase of SH (which scales with $T$); i.e., upwelling long wave radiation ($LW_{up}$) is partly playing the role in the energy balance that is played by SH in other regions. Adding changes in $LW_{up}$, Fig. 3e reproduces the pronounced

increases in the arid regions. Nevertheless, increases in $R_n$ in these arid regions are small and the surface energy balance ($R_n \approx \mathrm{SH} + \mathrm{LH}$) is still obeyed. The comparisons in Fig. 3abce here are consistent with and supplement the discussion of surface flux changes under different regimes of the temperature distribution change in Duan et al. (2020).

### *c. A discussion on the moisture constraint*

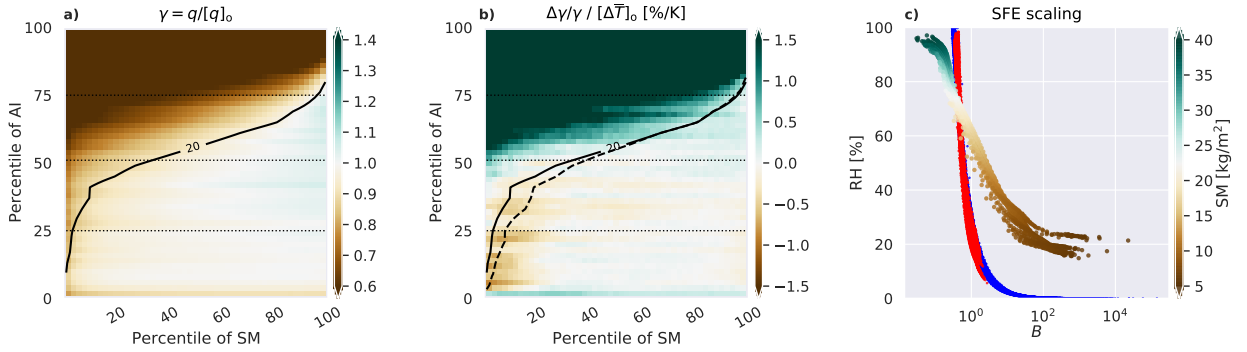


FIG. 4. (a) the land–ocean specific humidity ratio (the $\gamma$ in Byrne and O'Gorman (2013, 2018), calculated as the specific humidity $q$ at each land grid cell divided by the corresponding ocean zonal mean specific humidity $[q]_o$), (b) fractional changes in $\gamma$ normalized by $[\Delta\overline{T}]_o$, displayed in the phase space of daily soil moisture percentiles (horizontal axis), and climatological Aridity Index percentiles (vertical axis). The black contour is the isoline of the surface soil moisture value of 20 kg/m$^2$. (c) RH and the Bowen ratio $B$. Each dot represents one bin among the $50 \times 50$ spatial-temporal bins in the AI/SM phase space as in Fig. 3 and 5, and is color-coded by its SM value in the base climate. The blue/red dots in panel (c) show the theoretical scaling by the Surface Flux Equilibrium, red using RH to calculate $B$ and blue using $B$ to calculate RH. See text for more details.

As mentioned in Sections 1 and 3a, the stronger warming predicted over land in the QE–WTG framework emerges from the moisture constraint that $\Delta q^L = \gamma \Delta q^O$, which is derived based on the transport of atmospheric moisture from the ocean (Byrne and O'Gorman 2016; Chadwick et al. 2016). While the derivation of this moisture constraint emphasizes ocean control – specific humidity over land is assumed to follow specific humidity over ocean, which increases with warming approximately at the rate of the Clausius-Claperon scaling – land specific humidity is also affected by land-atmosphere exchanges (e.g. Van der Ent et al. 2010). A drier land surface will tend to result in lower evapotranspiration and, for a given amount of moisture convergence (although the two do not operate independently), a smaller $\gamma$. When the moisture constraint is

applied to climate model simulations, the value of $\gamma$ is calculated as the local climatological $q^L$ at each land grid cell divided by the corresponding zonal mean $q^O$ (Byrne and O′Gorman 2016, 2018), and is spatially-variable. Therefore, the moisture constraint (atmospheric perspective) contains information of the spatially-variable surface dryness (surface perspective). Note that the results in Byrne and O′Gorman (2016, 2018) were presented as averages over latitudinal bands or the entire 40°S–40°N domain, which is an average across the underlying variability of $\gamma$.

We use the same method as in Byrne and O′Gorman (2016, 2018) to calculate $\gamma$ on each day, and present its spatiotemporal distribution in the SM/AI phase space in Fig. 4a. Examining across the spatiotemporal distribution, $\gamma$ ranges from less than 0.2 in the very arid regions to about 1.2 in the wettest days (high local SM percentiles) in semi-arid and semi-moist regions. The lowest row (the lowest AI percentile bin) contains many grid cells in the upwind slope of the Tibetan Plateau where it rains heavily from the orographic lifting; therefore AI is small (AI $\propto R_n/P$) but the specific humidity (and $\gamma$) is not necessarily high (since temperature is low at high orographic altitude).

Under climate change, the moisture constraint assumes that the ratio $\gamma$ remains constant, but this may not hold if evapotranspiration changes are substantial and not compensated by changes in moisture convergence. The change in $\gamma$ is shown in Fig. 4b. We first draw the readers' eye to the decrease of $\gamma$ aligning along the critical soil moisture lines where changes in surface conditions are the strongest as emphasized by the surface perspective (see Section 3b). In Fig. 4b, for each degree warming, $\gamma$ decreases by about 1% in the water-limited transitional regime for the CMIP6 multi-model mean. This suggests that, when $q^O$ increases by 7%/K, $q^L$ in these conditions, due to the decrease of $\gamma$, will increase by 6%/K (taking the log and then taking the climate change difference on both sides of $q^L = \gamma q^O$ yields $\Delta q^L/q^L = \Delta q^O/q^O + \Delta\gamma/\gamma$). For $q^L \approx 16$ g/kg ($L_v q^L \approx 40$ kJ/kg, see Fig. A1c), the 1% change in $\gamma$ will produce a deviation of about 0.4 kJ/kg in $L_v \Delta q^L$ (which, assuming an accurate constraint of ΔMSE by QE and WTG, leads to a 0.4 K deviation in the prediction of $\Delta T^L$), for each degree of ocean mean warming. In applying the QE-WTG framework to predict the magnitude of land warming, this deviation brought by the moisture constraint assumption will partly compensate the deviation brought by the equal MSE assumption (the MSE increase in these conditions is smaller, see Fig. 2a and f). Note that in these transitional conditions where $\gamma$ decreases, LH also decreases (Fig. 3c). While we do not perform a moisture budget analysis here, this correspondence suggests the role of changing land-sourced

moisture in controlling changes in $\gamma$. In Byrne (2021) which applies the QE-WTG framework to discuss warming of the upper temperature percentiles, both the drier base-climate $q$ and a decrease of RH on those high temperature percentile days contribute to the amplified warming, and both of these have connections to the land surface.

Another domain in the phase space in Fig. 4b that shows perceptible changes in $\gamma$ is over the arid land regions: $\gamma$ increases by a much larger fractional rate. The driving mechanism for this increase is not yet clear: at the top soil moisture percentiles in these arid regions, both rainfall and LH (see Fig. 3c) increase; the overall increase in $\gamma$ and the moistening at the top soil moisture percentiles in these arid regions can result from both changes in the transport of moisture and local evapotranspiration.

While the atmospheric community conceptually emphasize the ocean control on $\gamma$ as discussed above, the land community emphasizes the land control. In particular, the theory of "Surface Flux Equilibrium" (SFE) from the land community (McColl et al. 2019; McColl and Rigden 2020) derived that

$$\mathrm{RH} = \frac{c_p}{L_v \phi} \frac{1}{B} \tag{9}$$

where $\phi$ is the derivative of saturation specific humidity $q^*(T)$ with respect to temperature ($\phi = \frac{\partial q^*}{\partial T}|_{T_{BL}} = \frac{L_v q^*}{R_v T_{BL}^2}$). This SFE is derived with the assumption that the boundary-layer RH is in equilibrium at and beyond daily timescales and the surface heating from SH balances surface moistening from LH (i.e., other sources and sinks for the BL heat and moisture budgets are neglected). The implication of SFE (Eq. 9) is that, if we know the Bowen ratio, we can know the boundary layer RH, and vice versa.

Boundary layer RH in the base climate can be effectively regarded as an key indicator for the warming/moistening partition in the atmospheric perspective, similar to $\gamma$: while $\gamma$ is the key parameter in the mathematical form of the QE–WTG framework, the physical intuition for the importance of base climate moisture in controlling warming magnitude draws upon the cloud-base height above which the temperature lapse rate shifts to follow a moist adiabat from a dry adiabat (see Fig. 1b). The cloud-base height is tightly related to the boundary-layer RH (Betts 2009), and therefore the base climate state of both can be regarded as the key control for the warming magnitude under the atmospheric perspective. In fact, when Byrne and O′Gorman (2013) first formed the QE-WTG framework based on equal equivalent potential temperature $\theta_e$ over land and

ocean, the decomposition for the land/ocean warming ratio was based on RH. Altogether, the SFE relation in Eq. 9 that directly associates RH with the Bowen ratio, is directly relating the key control in the atmospheric perspective to the key control in the surface perspective.

Fig. 4c shows the relationship between RH and the Bowen ratio $B$ for each box in the SM/AI phase space, with the color indicating the soil moisture. RH shows an inverse relationship with $B$, as expected. This inverse relationship suggest a strong land surface origin for the boundary layer RH: the surface influences RH through both controlling the source of water vapor through evapotranspiration and affecting temperature. The red and blue dots in Fig. 4c show the results when assuming SFE (Eq. 9; red dots use RH to calculate $B$ and blue dots use $B$ to calculate RH). SFE qualitatively captures the inverse relationship between RH and $B$, but there are notable deviations from what is simulated by the climate models, which likely result from the assumptions made in the derivations of SFE, although uncertainties of model parameterization of surface fluxes may have also contributed. For example, in wet conditions (green dots in Fig. 4c), SFE-based RH is higher than the actual RH, since moisture would likely be transported out of the boundary layer. In dry conditions (brown dots in Fig. 4c) SFE-based RH is lower than the actual RH because water vapor can be transported into dry regions. Contributions from these non-surface processes would moderate the atmospheric RH for a given Bowen ratio. While some of these correspondences may seem intuitive, we make them explicit because soil moisture and its changes do not appear directly in the QE-WTG framework, while studies based on the surface flux perspective do not typically rely on the behavior of the large-scale transport of moisture.

## 4. Base-climate sensitivity and changes in partition in the two perspectives

To what extent can the two perspectives explain the spatiotemporal warming pattern over land in climate models? Recall that in Section 2, we derived a relationship between the magnitude of warming in each perspective and three components: changes of the total energy/energy flux, the base-climate partition between the temperature and the moisture component (the inverse of which is termed the base-climate sensitivity), and the changes in this base-climate partition (Eqns. (6), (7)). The comparison of various relations for the two perspectives is listed in Table 1. In the following we examine the spatiotemporal distribution of the base-climate partition and its changes under warming, and the contribution of the base-state partition versus its changes to the warming

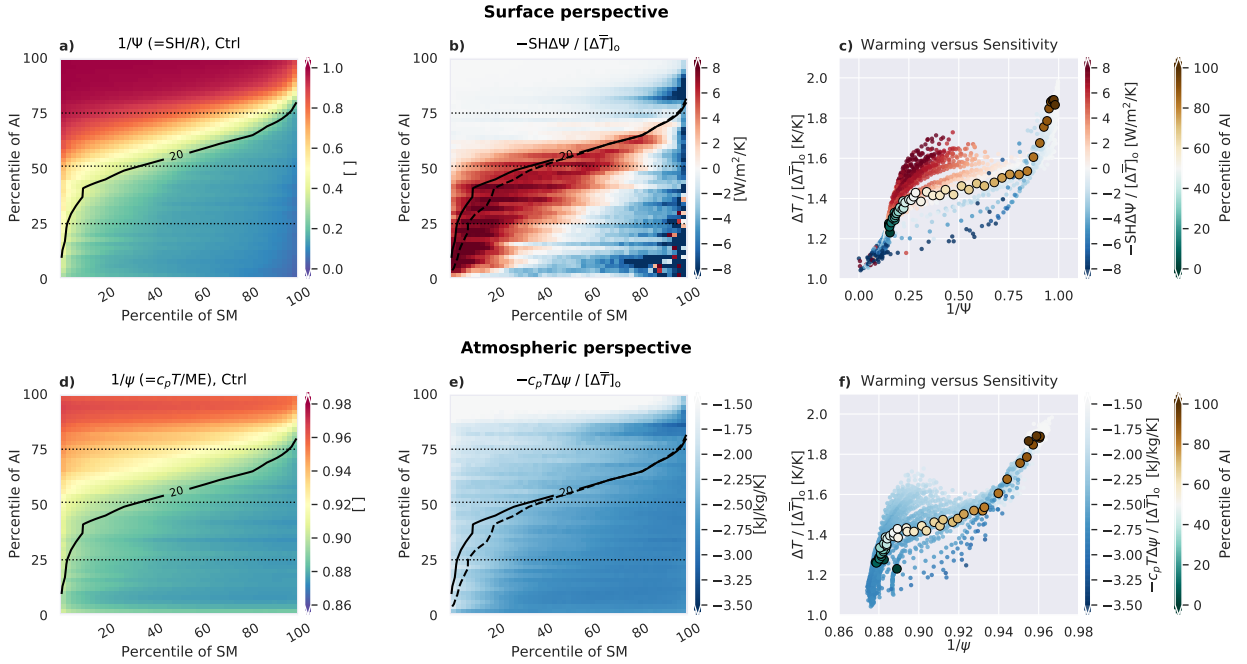


534 FIG. 5. (a, d) the base-climate sensitivity ($1/\Psi$ and $1/\psi$), (b, e) the repartition term ( $-\mathrm{SH}\Delta\Psi$ and $-c_pT\Delta\psi$;
535 a positive sign corresponds to a repartition towards enhancing warming), and (c, f) the relationship between
536 the magnitude of warming $\Delta T$ (normalized by mean tropical ocean warming $[\Delta T]_o$) and the base climate
537 sensitivity in the surface (c) and the atmospheric (f) perspectives. Small dots in (c) and (f) represent the $50\times50$
538 spatiotemporal bins, and are color-coded by the repartition terms as shown in (b) and (e); large dots in (c) and (f)
539 are the temporally-averaged values of warming and base-climate sensitivity for the 50 spatial bins, color-coded
540 by percentiles of the aridity index (AI).

549 magnitude. This alternative way of decomposition provides us a complementary view of the two
550 perspectives.

551 Figures 5a and d show the spatiotemporal distribution of the base-climate sensitivity. For
552 both the surface (Fig. 5a) and the atmospheric (Fig. 5d) perspectives, the base-climate sensitivity
553 is larger for drier conditions (upper-left) and smaller for wetter conditions (lower-right). Recall
554 that in the surface perspective, base-climate sensitivity $\Psi^{-1} = \mathrm{SH}/R \approx \mathrm{SH}/R_n$ is the ratio of
555 the surface sensible heat flux to the total net radiation; and in the atmospheric perspective, base-
556 climate sensitivity $\psi^{-1} = c_pT/\mathrm{ME}$ is the ratio of the temperature component of energy (dry specific
557 enthalpy) to the total moist enthalpy. Both reflect the dryness in the base climate, because they
558 indicate how much of the available energy/energy flux is partitioned into temperature/heating rather

than moisture/evapotranspiration. The correlation between the atmospheric and surface sensitivity is high (0.99, see also Fig. 6a), reflecting the tight connection of the two perspectives in the base climate.

The surface sensitivity $1/\Psi$ (Fig. 5a) ranges from 0 to 1: values over the desert are close to 1, indicating that $R_n$ at the surface is almost entirely balanced by SH; values in very high SM percentiles over moist and semi-moist regions are close to 0, indicating that $R_n$ is almost entirely balanced by LH. The atmospheric sensitivity $1/\psi$ (Fig. 5d), however, has a smaller range and is generally higher than the surface sensitivity (ranges from 0.88 for moist regions to 0.96 for arid regions). This indicates that in one climate state, for a given location, the near surface dry specific enthalpy ($c_pT$ around 300 kJ/kg, see Fig. A1b in Appendix A) dominates the total moist static energy (around 325 in arid regions to 345 kJ/kg in moist regions, see Fig. A1a). This is in contrast to the *variability* across the spatiotemporal distribution, and the *climate change* values, for which the latent energy ($L_vq$) values dominate those in surface air MSE.

Fig. 5b and e show the repartition term in Eq. 6 and Eq. 7. The repartition term captures the contribution of changes in the partition factor ($\psi$ and $\Psi$) to warming. The patterns of the repartition terms $-c_pT\Delta\psi$ and $-\mathrm{SH}\Delta\Psi$ are dominated by the patterns of changes in the partition factor $-\Delta\Psi$ and $-\Delta\psi$ (compare Fig. 5be with Fig. B1dc in Appendix B). In the surface perspective, the surface flux partitions towards higher latent heat flux under wet conditions (blue shadings in Fig. 5b) and towards higher sensible heat flux under intermediate (transitional and some wet) conditions (red shadings in Fig. 5b). Under dry conditions, changes in the partition factor are small, as are changes in SH and LH, except at the high soil moisture percentiles associated with rainy conditions.

The behavior of the repartition term in the atmospheric perspective contrasts with its behavior in the surface perspective: the atmospheric partition factor changes towards moistening under *all* conditions, although the magnitude of the repartition towards moisture is smallest in dry conditions in correspondence with the surface flux perspective (Fig. 5e). The inconsistency of the pattern in Fig. 5e compared to that in Fig. 5b reflects that, the atmosphere is responding to changes in land surface ET, but is generally getting moister under the influence of ocean as the globe warms. There is also a possible contribution from changes in the evaporation of precipitation, since it is a source of boundary layer specific humidity.

Having established the spatiotemporal structure of the key terms in our diagnostic equations, we test their relationship to the warming magnitude. Fig. 5c and f shows the warming magnitude in each of the $50 \times 50$ bins as a function of the base-climate sensitivity, with the small dots color coded by the repartition term. This clearly demonstrates the relationship between the warming magnitude and the base-climate sensitivity in both perspectives: higher base-climate sensitivity (drier base-climate conditions) leads to a larger magnitude of warming. The larger dots show the temporally-averaged values of warming and base-climate sensitivity across the 50 AI bins, color-coded by the percentile of AI in each spatial bin. Here, we also see that climatologically arid regions warm the most and climatologically moist regions warm the least.

Eq. 6 and Eq. 7 suggest that if $\Delta R_n$ and $\Delta$MSE are relatively uniform, and the repartition term is close to zero, the warming magnitude will scale linearly with the base-climate sensitivity. In Fig. 5c and f, we indeed see the general linear increase of $\Delta T$ with $1/\Psi$ and $1/\psi$. However, during the intermediate conditions between the very wet and dry (those with a surface sensitivity of $0.2 \leq 1/\Psi \leq 0.8$, and an atmospheric sensitivity of $0.88 \leq 1/\psi \leq 0.93$), there is a spread in $\Delta T$ at a given base climate sensitivity. This spread is consistent with the repartition terms (color shading of the dots). In these intermediate conditions, when surface flux partitions towards SH (red dots in Fig. 5c), the warming magnitude is amplified. Conversely, when surface flux partitions towards the LH (blue dots in Fig. 5c), the warming magnitude is dampened.

The similar and quasi-linear relationship (especially for the time-mean; the large dots in Fig. 5cf) between the warming magnitude and the base-climate sensitivity in both perspectives indicates that in climate models, the climatological dryness, both for the surface and the atmosphere, largely explains the spatial pattern of the warming magnitude. This is to say, we do not need drying of soil to explain the approximate spatial distribution of the *mean* warming. However, drying of soil and changes in the surface flux partition is important to explain the variability of warming at shorter time scales, especially during intermediate conditions between wet and dry.

## 5. Discussion: the lower tropospheric temperature lapse rate and the surface fluxes

The atmospheric perspective is top-down: starting from the same temperature in the free troposphere constrained by WTG and moving downward, a larger mean lapse rate has to be associated with a higher surface air temperature, as well as a larger magnitude of surface air warming for a

given change in free tropospheric temperatures. Fig. 6c shows the temperature profiles over a few regions of different surface aridity in CMIP6 models for the base climate. They are, from moist to arid: the ocean averaged over the tropics (blue), the Amazon forest (green), the land averaged over the tropics (black), and the Sahara desert (orange). In the free troposphere (above roughly 3 km), the temperature over the different regions is relatively uniform, and approximately follows the moist adiabat (the dashed pink line), as assumed in both Joshi et al. (2013) and the QE–WTG framework. In the lower troposphere, the temperature lapse is indeed closer to a dry adiabat for more arid regions, and closer to a moist adiabat for more moist regions, although in all cases the simulated lapse rate falls between these two edge cases. Note that the QE–WTG schematic (Fig. 1b; Byrne and O′Gorman 2013) is comparable to the lapse rate schematic (Fig. 1a; Joshi et al. 2013) and the CMIP6-based lapse rates (Fig. 6c) because the higher the cloud base, the longer path in the lower troposphere where temperature follows the dry adiabat, the larger the mean lapse rate in the lower troposphere. In this context, the lower tropospheric lapse rate, the cloud base height, and the boundary layer RH are closely related, and variously act as the key control for the warming magnitude in the atmospheric perspective.

The surface perspective is bottom-up: temperature increases more when SH is higher for a given change in $R_n$. Fig. 6b shows a strong positive relationship between the mean temperature lapse rate in the lower troposphere and the ratio of SH to total turbulent flux $R$ (SH/$R$, our base-climate sensitivity), where $R = R_n - G = \mathrm{SH} + \mathrm{LH} \approx R_n$. The outliers in the figure are the 50 temporal bins in the first AI bin, which are located at the edge of the Tibetan Plateau around Nepal. As mentioned in the context of Fig. 4a, this region has a very small AI due to a large amount of orographic precipitation, but the high orographic altitude makes the temperature lapse rate between 700 hPa and the surface small, since the level of 700 hPa is within the boundary layer. We can qualitatively understand the connection between the lapse rate and SH/$R$ as follows: in drier regions, SH is a higher fraction of $R$, so the energy received by the surface is turbulently diffused into the boundary layer rather than (potentially) transported out as water vapor. In addition, drier regions also have less horizontal moisture convergence in the lower troposphere, which is associated with less rain. Higher SH and lack of rain at the surface result in a warmer surface air relative to aloft; combined with WTG in the free troposphere, the warmer surface air over drier regions yields a larger mean temperature lapse rate in the lower troposphere.

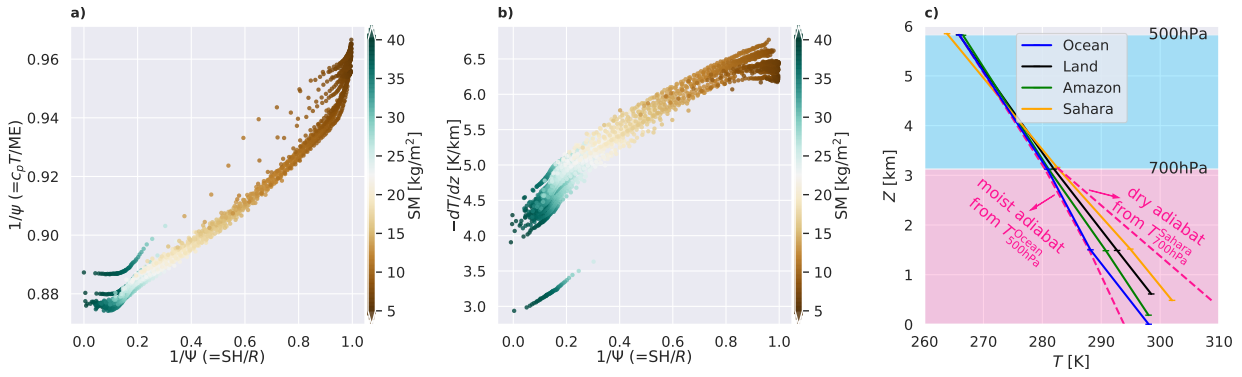


FIG. 6. The relationship between the base-climate (a) atmospheric sensitivity $1/\psi$ and surface sensitivity $1/\Psi$, (b) temperature lapse rate between the 700 hPa level and the near surface level ($-dT/dz$) and surface sensitivity $1/\Psi$ (the fraction of SH in the total enthalpy flux $R$), and (c) warm season mean temperature profiles during 1850–1879 from CMIP6 models (see Section 2 for details), averaged over tropical (30S–30N) ocean (blue), tropical land (black), Amazon forest (15°S-0°, 70°W-55°W; green) and Sahara desert (20°N-30°N, 10°E-30°E, orange). The two pink dashed lines in panel c illustrate the temperature profile below 700 hPa if following the dry adiabat (right side, starting with temperature at 700 hPa over the Sahara desert and integrating downward), and the temperature profile below 500 hPa if following the moist adiabat (left side, starting with temperature at 500 hPa averaged over the tropical ocean and integrating downward).

## 6. Summary and outlook

Motivated to better understand the amplified warming over tropical land and its association with dry conditions, we compare the two existing perspectives in the field that aim to explain the "drier–warmer" phenomenon. One is based on the atmospheric dynamics of the tropical troposphere (the atmospheric dynamics perspective), and the other focuses on land surface processes (the surface flux perspective). The atmospheric dynamics perspective uses moist static energy as a constrained quantity, and derives the amplified warming from lower (base-climate) specific humidity. The surface flux perspective uses the net radiation at the surface as a constrained total, and centers its argument on reduced water availability due to soil drying and/or plant-moderated reductions in transpiration, which results in a change in the partitioning between the sensible and the latent heat fluxes.

Based on climate model outputs, we first present a comparison of the full spatiotemporal distribution of the relevant variables in the two perspectives in the AI/SM phase space (Fig. 2 and 3) and

discuss the applicability of the equal MSE assumption in the QE-WTG framework in explaining the spatiotemporal variability. By comparing the full spatiotemporal distribution, we address the first question we raise in the beginning on how key variables in the two perspectives correspond to each other. We also examine the connection of the moisture constraint in the atmospheric perspective to surface conditions, where we show how the neglect of changes in local evapotranspiration in the atmospheric perspective and the neglect of atmospheric processes in the surface perspective may lead to deviations (Fig. 4). From here, we can better understand the second question we raise, how the dryness measures between the two perspectives relate to each other. We then use a diagnostic linearized perturbation framework to relate the temperature response to a base-climate sensitivity, changes in the MSE or $R_n$, and changes in the warming versus moistening partition factor. We show that the base climate sensitivity largely explains the warming magnitude across spatiotemporal conditions: drier base-climate conditions have a larger base-climate sensitivity and experience a larger magnitude of warming. This relationship between the warming magnitude and the base-climate sensitivity holds particularly well for the time mean, and the surface and the atmospheric perspectives correspond well in terms of this role of the base-climate sensitivity. On top of the quasi-linear relationship between the warming magnitude and the base-climate sensitivity, changes in the partition factor between warming and moistening for intermediate (between wet and dry) conditions further enhance or dampen the warming magnitude (Fig. 5). This informs us on the third question we raise, how climatological dryness versus changes in dryness contribute to amplified warming in each perspective. Lastly, through linking the lower tropospheric lapse rate with the surface fluxes (Fig. 6), we provide mechanistic insights on how the top-down atmospheric perspective connects with the bottom-up surface perspective. The comparison of the two perspectives in our study reveals how key arguments of the two perspectives hold across the spatiotemporal conditions and advances our understanding of the drier-warmer relationship. Our analyses are based on CMIP6 model output and are largely diagnostic; comparisons with observations and further quantifying the contribution from specific land surface and atmospheric processes can be informative.

*Acknowledgments.* The authors acknowledge the support from the NSF grant 1939988. We thank three anonymous reviewers for helpful reviews and the editor for handling the manuscript. S.Q.D. appreciates helpful conversations with Dr. Zhihong Tan and Dr. Mengxi Wu. The authors also acknowledge the World Climate Research Programme, which, through its Working Group on Coupled Modelling, coordinated and promoted CMIP6. We thank the climate modeling groups for producing and making available their model output, the Earth System Grid Federation (ESGF) for archiving the data and providing access, and the multiple funding agencies who support CMIP6 and ESGF. I.R.S. acknowledges funding from the National Center for Atmospheric Research, which is a major facility sponsored by the National Science Foundation under the Cooperative Agreement 1852977.

*Data availability statement.* CMIP6 model outputs used in this study can be downloaded from the CMIP6 data archive (https://esgf-node.llnl.gov/search/cmip6/). ERA5 reanalysis data can be downloaded from the ECMWF Climate Data Store (https://cds.climate.copernicus.eu/). Jupyter Notebooks for analyzing the data will be shared through GitHub at the acceptance of this paper.

# APPENDIX A

## Spatiotemporal distribution of relevant variables in the base climate state

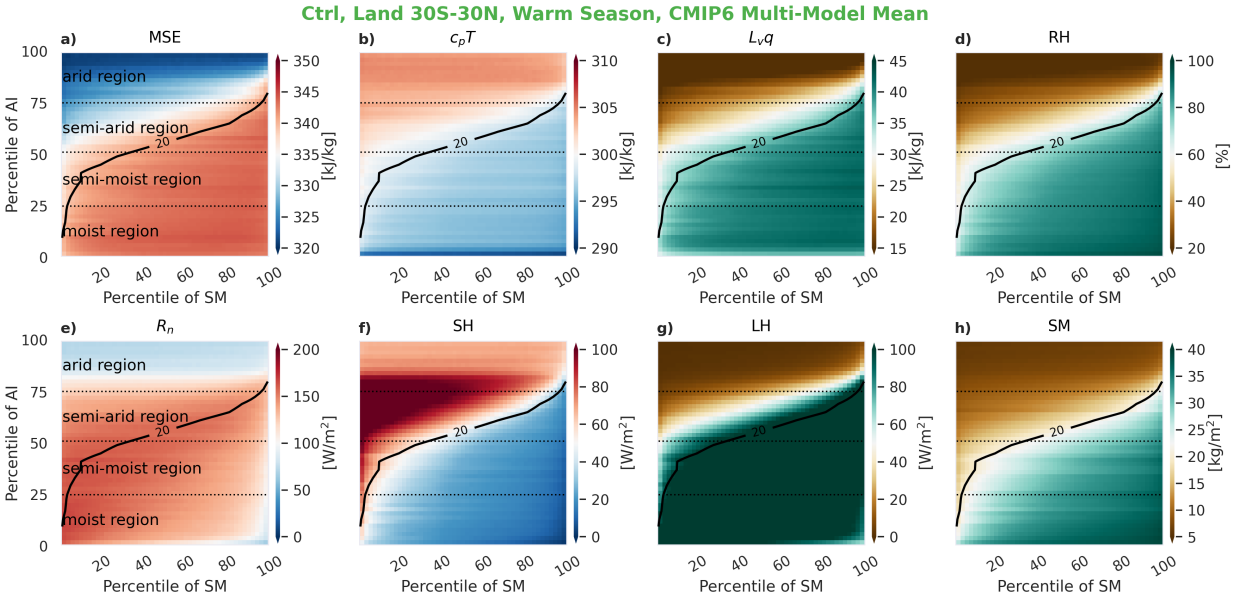


712 FIG. A1. The spatiotemporal distribution of the base-climate surface air (a) moist static energy (MSE), (b)
713 temperature converted to energy units ($c_pT$), (c) specific humidity converted to energy units ($L_vq$), (d) relative
714 humidity (RH), and the surface (e) net radiation ($R_n$), (f) sensible heat flux (SH), (g) latent heat flux (LH), (h)
715 soil moisture (SM) in the phase space of daily soil moisture percentile and climatological aridity index (AI)
716 percentile. The black contour shows the critical SM of 20 kgm$^{-2}$.

717 # APPENDIX B

718 ## Additional information for terms in the diagnostic perturbation equations

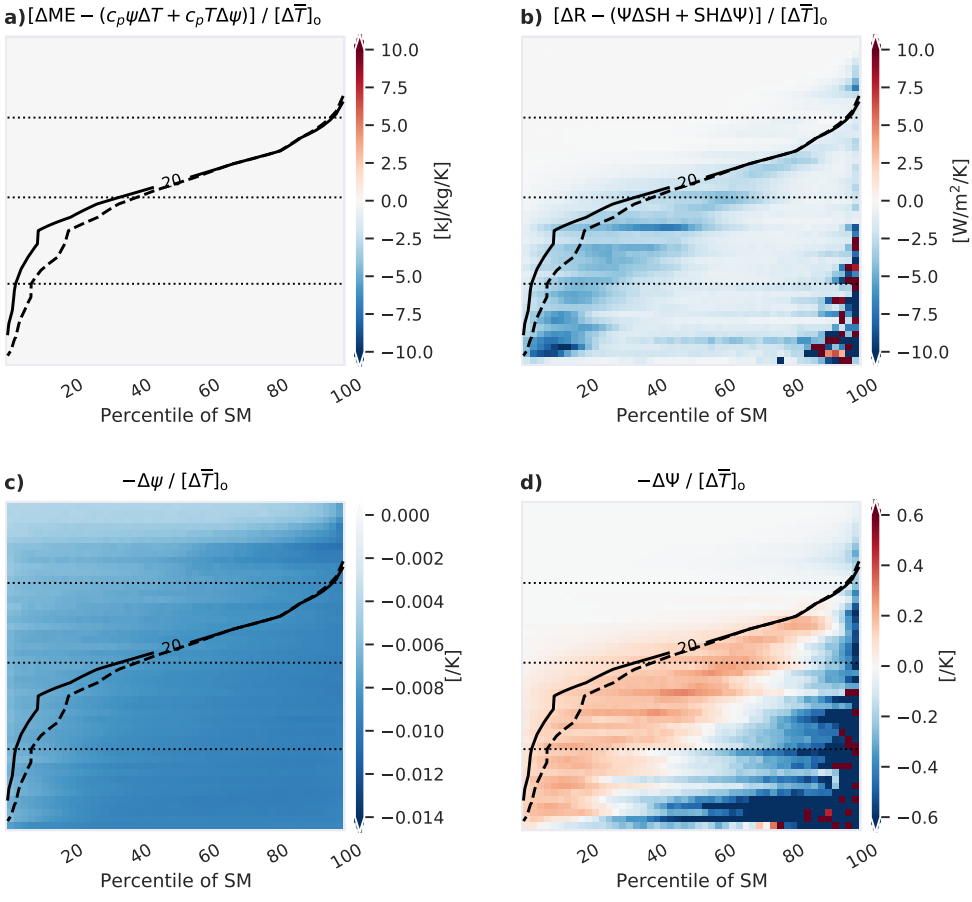


719 FIG. B1. (a) The residuals from the linearization in Eq. 3; (b) the residuals from the linearization in Eq. 4;
720 (c) changes in the atmospheric partition factor $-\Delta\psi$; (d) changes in the surface partition factor $-\Delta\Psi$. The fact
721 that the patterns in (c) and (d) are similar to patterns in Fig. 5be indicates that the spatiotemporal distribution
722 of changes in the partition factor ($-\Delta\psi$ and $-\Delta\Psi$) dominates the spatiotemporal distribution of the repartition
723 terms ($-c_p T\Delta\psi$ and $-\mathrm{SH}\Delta\Psi$).

724 # APPENDIX C

725 ## The relationship between perturbations in the surface sensible heat flux and perturbations
726 ## in temperature

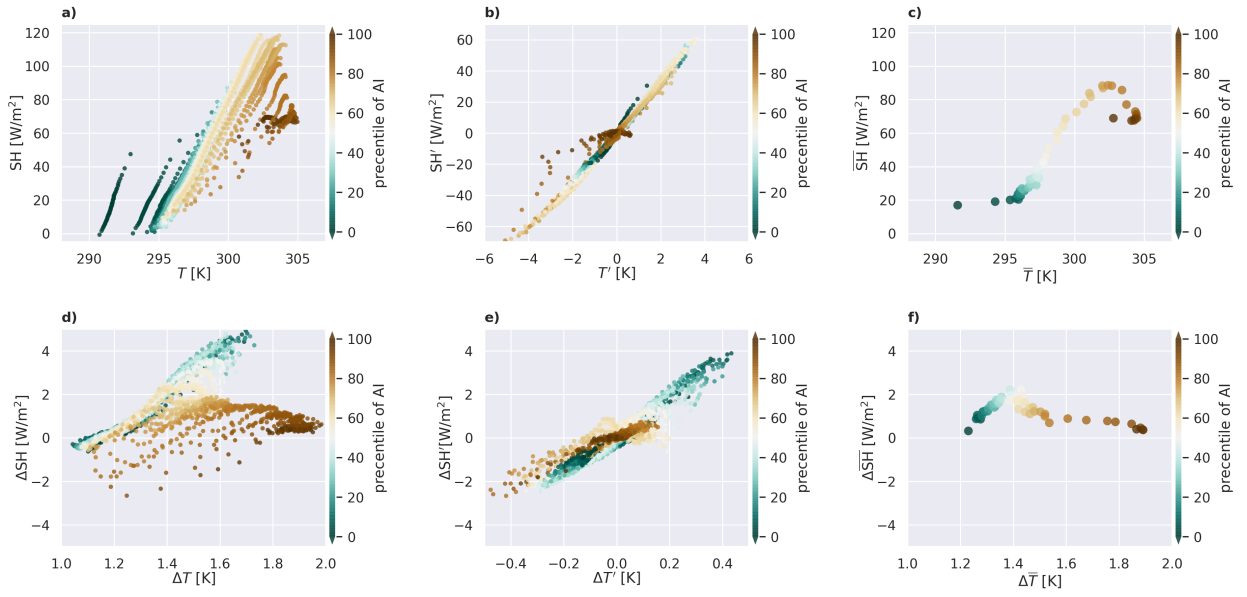


FIG. C1. The relationship between (a) the base-climate surface sensible heat flux (SH) and surface air temperature ($T$); (b) the base-climate temporal anomalies in SH and $T$, with the local temporal-mean value removed, (c) the local temporal-mean SH and $T$; (d) the climate changes in SH and $T$; (e) the temporal anomalies of changes in SH and $T$ with the local temporal-mean change removed; (f) the local temporal-mean changes in SH and $T$. All scatters are color-coded by the percentile of the aridity index (AI). In panels a, b, d, and e, each scatter represents one of the $50 \times 50$ spatio-temporal bins, and in panels c and f, each scatter represents one of the 50 spatial bin, with the temporal dimension averaged out.

In the perturbation relation we use for the surface energy balance (Eq. 5), we have linearized the perturbation in the surface sensible heat flux (SH) as a coefficient $\kappa$ times the temperature perturbation. Fig. C1 examines to what extent this linearization is justifiable.

The first row shows the relationships between SH and $T$ in the base climate. Panel b informs us that temporal perturbations in SH and $T$ relate to each other linearly by a similar coefficient (approximately 15–20 W/m$^2$/K) across locations, except in the very dry locations. Panel c informs us that spatial anomalies of the mean SH and $T$ also relates to each other linearly except the very moist and very dry locations.

The second row shows the relationships between changes in SH and $T$ under climate change. For our particular application of the linearized perturbation relation Eq. 5, panel (d) is the most relevant. It shows us that for moist and semi-moist conditions, $\Delta$SH and $\Delta T$ have relatively good

linear relationship, while the relationship for dry regions is weaker. If we remove the mean at each location and only focus on the temporal anomalies, then all locations show a linear relationship (panel e), with the regression coefficient, i.e., $\kappa$, being approximately 5 W/m$^2$/K for dry locations and 10 W/m$^2$/K for moist locations. There is no linear relationship between the time-mean change in SH and $T$ across locations (panel f).

Since in our analysis, the data we use retains the temporal variability and we emphasize the qualitative understanding, we accept simply linearizing $\Delta$SH as $\kappa\Delta T$. With this linearization we can derive Eq. 7, and we have the surface sensitivity as $1/(\kappa\Psi)$. We assume $\kappa$ is the same constant across spatiotemporal conditions and focus on the sensitivity factor $1/\Psi$. The non-uniformity of $\kappa$ will make quantitative predictions of the warming magnitude more complicated; although here we see that it may be approached by separating dry and moist conditions.

## References


Arakawa, A., and W. H. Schubert, 1974: Interaction of a cumulus cloud ensemble with the large-scale environment, Part I. *Journal of the atmospheric sciences*, **31 (3)**, 674–701.

Berg, A., B. R. Lintner, K. L. Findell, S. Malyshev, P. C. Loikith, and P. Gentine, 2014: Impact of soil moisture–atmosphere interactions on surface temperature distribution. *Journal of Climate*, **27 (21)**, 7976–7993.

Betts, A. K., 2009: Land-surface-atmosphere coupling in observations and models. *Journal of Advances in Modeling Earth Systems*, **1 (3)**.

Byrne, M. P., 2021: Amplified warming of extreme temperatures over tropical land. *Nature Geoscience*, **14 (11)**, 837–841.

Byrne, M. P., and P. A. O′Gorman, 2013: Land–ocean warming contrast over a wide range of climates: Convective quasi-equilibrium theory and idealized simulations. *Journal of Climate*, **26 (12)**, 4000–4016.

Byrne, M. P., and P. A. O′Gorman, 2016: Understanding decreases in land relative humidity with global warming: Conceptual model and GCM simulations. *Journal of Climate*, **29 (24)**, 9045–9061.

Byrne, M. P., and P. A. O′Gorman, 2018: Trends in continental temperature and humidity directly linked to ocean warming. *Proceedings of the National Academy of Sciences*, 201722312.

Chadwick, R., P. Good, and K. Willett, 2016: A simple moisture advection model of specific humidity change over land in response to SST warming. *Journal of Climate*, **29 (21)**, 7613–7632.

Chan, D., A. Rigden, J. Proctor, P. W. Chan, and P. Huybers, 2022: Differences in radiative forcing, not sensitivity, explain differences in summertime land temperature variance change between CMIP5 and CMIP6. *Earth's Future*, **10 (2)**, e2021EF002 402.

Dirmeyer, P. A., G. Balsamo, E. M. Blyth, R. Morrison, and H. M. Cooper, 2021: Land-atmosphere interactions exacerbated the drought and heatwave over northern europe during summer 2018. *AGU Advances*, **2 (2)**, e2020AV000 283.

Donat, M. G., A. J. Pitman, and S. I. Seneviratne, 2017: Regional warming of hot extremes accelerated by surface energy fluxes. *Geophysical Research Letters*, **44 (13)**, 7011–7019.

Duan, S. Q., K. L. Findell, and S. A. Fueglistaler, 2023: Coherent mechanistic patterns of tropical land hydroclimate changes. *Geophysical Research Letters*, **50 (7)**, e2022GL102 285.

Duan, S. Q., K. L. Findell, and J. S. Wright, 2020: Three regimes of temperature distribution change over dry land, moist land and oceanic surfaces. *Geophysical Research Letters*, e2020GL090997, https://doi.org/https://doi.org/10.1029/2020GL090997.

Emanuel, K. A., J. David Neelin, and C. S. Bretherton, 1994: On large-scale circulations in convecting atmospheres. *Quarterly Journal of the Royal Meteorological Society*, **120 (519)**, 1111–1143.

Eyring, V., S. Bony, G. A. Meehl, C. A. Senior, B. Stevens, R. J. Stouffer, and K. E. Taylor, 2016: Overview of the Coupled Model Intercomparison Project Phase 6 (CMIP6) experimental design and organization. *Geoscientific Model Development*, **9 (5)**, 1937–1958.

Fu, Q., and S. Feng, 2014: Responses of terrestrial aridity to global warming. *Journal of Geophysical Research: Atmospheres*, **119 (13)**, 7863–7875.

Held, I. M., and K. M. Shell, 2012: Using relative humidity as a state variable in climate feedback analysis. *Journal of Climate*, **25 (8)**, 2578–2582.

Joshi, M., F. Lambert, and M. Webb, 2013: An explanation for the difference between twentieth and twenty-first century land–sea warming ratio in climate models. *Climate Dynamics*, **41 (7)**, 1853–1869.

Joshi, M. M., J. M. Gregory, M. J. Webb, D. M. Sexton, and T. C. Johns, 2008: Mechanisms for the land/sea warming contrast exhibited by simulations of climate change. *Climate Dynamics*, **30 (5)**, 455–465, https://doi.org/https://doi.org/10.1007/s00382-007-0306-1.

Kong, W., K. A. McKinnon, I. R. Simpson, and M. M. Laguë, 2023: Understanding responses of summer continental daily temperature variance to perturbations in the land surface evaporative resistance. *Journal of Climate*, **36 (6)**, 1653–1678.

Koster, R. D., and S. P. Mahanama, 2012: Land surface controls on hydroclimatic means and variability. *Journal of Hydrometeorology*, **13 (5)**, 1604–1620.

McColl, K. A., and A. J. Rigden, 2020: Emergent simplicity of continental evapotranspiration. *Geophysical Research Letters*, **47 (6)**, e2020GL087 101.

McColl, K. A., G. D. Salvucci, and P. Gentine, 2019: Surface flux equilibrium theory explains an empirical estimate of water-limited daily evapotranspiration. *Journal of Advances in Modeling Earth Systems*, **11 (7)**, 2036–2049.

Milly, P. C., and K. A. Dunne, 2016: Potential evapotranspiration and continental drying. *Nature Climate Change*, **6 (10)**, 946–949.

Neelin, J. D., and N. Zeng, 2000: A quasi-equilibrium tropical circulation model–formulation. *Journal of the atmospheric sciences*, **57 (11)**, 1741–1766.

Roe, G., 2009: Feedbacks, timescales, and seeing red. *Annual Review of Earth and Planetary Sciences*, **37 (1)**, 93–115.

Seneviratne, S. I., T. Corti, E. L. Davin, M. Hirschi, E. B. Jaeger, I. Lehner, B. Orlowsky, and A. J. Teuling, 2010: Investigating soil moisture–climate interactions in a changing climate: A review. *Earth-Science Reviews*, **99 (3-4)**, 125–161.

Sherwood, S., and Q. Fu, 2014: A drier future? *Science*, **343 (6172)**, 737–739.

Sobel, A. H., and C. S. Bretherton, 2000: Modeling tropical precipitation in a single column. *Journal of climate*, **13 (24)**, 4378–4392.

Sutton, R. T., B. Dong, and J. M. Gregory, 2007: Land/sea warming ratio in response to climate change: IPCC AR4 model results and comparison with observations. *Geophysical research letters*, **34 (2)**.

Van der Ent, R. J., H. H. Savenije, B. Schaefli, and S. C. Steele-Dunne, 2010: Origin and fate of atmospheric moisture over continents. *Water Resources Research*, **46 (9)**.

Vargas Zeppetello, L., and D. Battisti, 2020: Projected increases in monthly midlatitude summertime temperature variance over land are driven by local thermodynamics. *Geophysical Research Letters*, **47 (19)**, e2020GL090 197.

Vogel, M. M., R. Orth, F. Cheruy, S. Hagemann, R. Lorenz, B. Hurk, and S. I. Seneviratne, 2017: Regional amplification of projected changes in extreme temperatures strongly controlled by soil moisture-temperature feedbacks. *Geophysical Research Letters*, **44 (3)**, 1511–1519.

Zelinka, M. D., T. A. Myers, D. T. McCoy, S. Po-Chedley, P. M. Caldwell, P. Ceppi, S. A. Klein, and K. E. Taylor, 2020: Causes of higher climate sensitivity in CMIP6 models. *Geophysical Research Letters*, **47 (1)**, e2019GL085 782.

Zeppetello, L. V., É. Tétreault-Pinard, D. Battisti, and M. Baker, 2020: Identifying the sources of continental summertime temperature variance using a diagnostic model of land–atmosphere interactions. *Journal of Climate*, **33 (9)**, 3547–3564.

Zhang, Y., and S. Fueglistaler, 2020: How tropical convection couples high moist static energy over land and ocean. *Geophysical Research Letters*, **47 (2)**, e2019GL086 387.